materials

MDPI

Article

Two B-C-O Compounds: Structural, Mechanical Anisotropy and Electronic Properties under Pressure

Liping Qiao [1,*] and Zhao Jin [2]

[1] Team of Micro & Nano Sensor Technology and Application in High-altitude Regions, Xizang Engineering Laboratory for Water Pollution Control and Ecological Remediation, School of Information Engineering, Xizang Minzu University, Xianyang 712082, China

[2] School of Information Engineering, Chang'an University, Xi'an 710064, China; zhaojin@chd.edu.cn

* Correspondence: lpqiao@126.com or lpqiao@xzmu.edu.cn; Tel.: +86-29-3375-5448

Received: 16 October 2017; Accepted: 8 December 2017; Published: 11 December 2017

Abstract: The structural, stability, mechanical, elastic anisotropy and electronic properties of two ternary light element compounds, B_2CO_2 and $B_6C_2O_5$, are systematically investigated. The elastic constants and phonon calculations reveal that B_2CO_2 and $B_6C_2O_5$ are both mechanically and dynamically stable at ambient pressure, and they can stably exist to a pressure of 20 GPa. Additionally, it is found that B_2CO_2 and $B_6C_2O_5$ are wide-gap semiconductor materials with indirect energy gaps of 5.66 and 5.24 eV, respectively. The hardness calculations using the Lyakhov-Oganov model show that B_2CO_2 is a potential superhard material. Furthermore, the hardness of $B_6C_2O_5$ is 29.6 GPa, which is relatively softer and more easily machinable compared to the B_2CO_2 (41.7 GPa). The elastic anisotropy results show that $B_6C_2O_5$ exhibits a greater anisotropy in the shear modulus, while B_2CO_2 exhibits a greater anisotropy in Young's modulus at ambient pressure.

Keywords: B-C-O system; stability; mechanical properties; anisotropy; electronic properties

1. Introduction

It has been found that the light elements such as B, C, N, and O can form strong covalently bonded materials that show intrinsic superhard characteristics. A series of new B-C-O compounds with multifunctional properties similar to $B_{13}C_2$ [1,2], B_6O [2,3], B_4C [3], BC [4,5], B_2C [4,6], B_3C [4,7], BC_4 [4], B_4C [4], B_5C [4], B_2CO [8,9], and B_2C_2O, B_2C_3O, and B_2C_5O [10], B_4CO_4 [11,12], 2D B-C-O alloys [13], BC_xN [14–19], BCN [20–22], BN [20,23], B_xO [24–26] and C_xN_y [27–35] has been designed by the theoretical method. These materials are almost all superhard materials.

Using the developed particle swarm optimization (PSO) algorithm for crystal structure prediction, Wang et al. [4] explored the possible crystal structures of B-C systems that are mechanically and dynamically stable. They found that with the exception of B_4C and BC_4, all boron carbides have high shear moduli (more than 240 GPa), indicating their strong resistance to shape change at constant volume. Theoretical Vickers hardness calculations showed that these boron carbides are potential superhard materials because the predicted hardnesses exceed 40 GPa. Zhang et al. [20] designed different kinds of superhard materials using the Crystal structure AnaLYsis by Particle Swarm Optimization (CALYPSO) algorithm. They found superhard phases in binary B-N compounds (such as Pct-BN, *Pbca*, Z-BN, BC_8-BN, and M-BN) and ternary B-C-N compounds (such as *I*-4*m*2 BCN, *Imm*2 BCN [21], and *P*3*m*1 BCN [22]). *Pbca*-BN with an orthorhombic structure was investigated by first-principles calculations by Fan et al. [23], who found that *Pbca*-BN has the shear modulus of 316 GPa, bulk modulus of 344 GPa, large Debye temperature of 1734 K, and hardness of 60.1 GPa. Ternary B-C-N compounds *I*-4*m*2 BCN, *Imm*2 BCN, and *P*3*m*1 BCN were investigated by first-principles calculations by Fan et al. [21,22] and were all found to be potential superhard materials. Electronic structure studies showed that BCN materials in the *P*3*m*1 and *I*-4*m*2 phases are indirect semiconductors

with band gaps of 4.10 eV and 0.45 eV, respectively, while the *Imm*2 phase is a direct semiconductor with a band gap of 2.54 eV.

Recently, Zhang et al. [10] performed extensive structure searches to explore the potential energetically stable B_2C_xO ($x \geq 2$) phases at ambient pressure using the current developed CALYPSO algorithm. B_2C_2O, B_2C_3O, and B_2C_5O in the tetragonal $I4_1/amd$, I-4m2, and P-4m2 phases, respectively, were reported in ref. [10]. The phonon dispersion and formation enthalpy calculations revealed that B_2C_2O, B_2C_3O, and B_2C_5O are all dynamically stable and can be synthesized at ambient conditions. The hardnesses of B_2C_2O, B_2C_3O, and B_2C_5O are 57, 62, and 68 GPa using Gao's model [36], and they are all potential superhard materials. B_2CO, a potential superhard material in the B-C-O system, can stably exist in several different phases. tP4-B_2CO, with the P-4m2 phase and tI16-B_2CO with the I-42d phase have been reported by Li et al. [9], while oP8-B_2CO with the $Pmc2_1$ phase was systematically investigated by Liu et al. [8] The elastic constants, phonon dispersion spectra and formation enthalpies confirmed the mechanical, dynamical and thermodynamic stabilities, respectively, of oP8-B_2CO, tP4-B_2CO, and tI16-B_2CO. Calculation of the Vickers hardness of oP8-B_2CO shows that oP8-B_2CO is a superhard material, and the Vickers hardness of oP8-B_2CO (47.70 GPa) is much closer to tP4-B_2CO (49.24 GPa) and tI16-B_2CO (49.56 GPa). The band structure calculations illustrate that all B_2CO phases are semiconductor materials with indirect band gaps, and oP8-B_2CO has the widest band gap (3.540 eV), greater than those of tP4-B_2CO (1.658 eV) and tI16-B_2CO (2.988 eV).

B_4CO_4, found in the I-4 space group, is a novel tetragonal thermodynamically stable phase, and two low-enthalpy metastable compounds ($B_6C_2O_5$ in $P1$ phase, B_2CO_2 in $C2/m$ phase) have been discovered by Wang et al. [12] using the widely used and evolutionary Universal Structure Predictor: Evolutionary Xtallography (USPEX) algorithm. The structural, stability, mechanical, elastic anisotropy and electronic properties of B_4CO_4 have been systematically investigated as described in ref. [11,12]. However, the structural, stability, mechanical, and elastic anisotropy properties of B_2CO_2 and $B_6C_2O_5$ have not been reported. Therefore, in this work, we systematically investigate the structural, stability, mechanical, elastic anisotropy and electronic properties of B_2CO_2 and $B_6C_2O_5$.

2. Theoretical Methods

The calculations were performed using density functional theory with the exchange-correlation functional treated using the generalized gradient approximation (GGA) in the Perdew-Burke-Ernzerhof (PBE) form [37] and the Perdew-Burke-Ernzerhof for solids (PBEsol) form [38], and with local density approximation (LDA) based on the data of Ceperley and Alder as parameterized by Perdew and Zunger (CA-PZ) [39,40]. The calculations in this work were performed using the Cambridge Serial Total Energy Package (CASTEP) code [41]. Structural optimizations were conducted using the Broyden-Fletcher-Goldfarb-Shanno (BFGS) minimization algorithm [42]. A high-density k-point [43] sampling with a grid spacing of less than $2\pi \times 0.025$ Å^{-1} ($4 \times 16 \times 7$ for B_2CO_2, $9 \times 9 \times 9$ for B_2CO_2) in the Brillouin zone was used. The self-consistent convergence criterion for the total energy was 5×10^{-6} eV/atom, the maximum force on the atom was 0.01 eV/Å, the maximum ionic displacement was within 5×10^{-4} Å and the maximum stress was within 0.02 GPa. The HSE06 hybrid functional [44] was used for the calculations of electronic structures of B_2CO_2 and $B_6C_2O_5$.

3. Results and Discussion

3.1. Structural Properties

The crystal structures of B_2CO_2 and $B_6C_2O_5$ are shown in Figure 1a–d, respectively. For the structure shown in Figure 1a, there are two inequivalent oxygen atom positions (O1 in (0.1337, 0.0, 0.0474), red; O2 in (0.9735, 0.5, 0.2763), orange), two inequivalent boron atom positions (B1 in (0.8891, 0.0000, 0.2433), light green; B2 in (0.1298, 0.5000, 0.2027), dark green), and an equivalent carbon atom (C in (0.2497, 0.0000, 0.5855), blue) in B_2CO_2. In the structure shown in Figure 1c, each atom occupies a different position in $B_6C_2O_5$ (B in (0.4165, 0.5981, 0.0121), (0.6796, 0.1566, 0.1255), (0.9807, 0.7214,

0.2895), (0.5464, 0.8782, 0.5674), (0.3288, 0.3515, 0.4784) and (0.1293, 0.0127, 0.8430); C in (0.4451, 0.9082, 0.8863) and (0.3015, 0.6221, 0.3228); and O in (0.5669, 0.1822, 0.4377), (0.8809, 0.8281, 0.5836), (0.7350, 0.4833, 0.0788), (0.9854, 0.0320, 0.1394), and (0.2105, 0.3326, 0.7576)). The calculated lattice parameters of B_2CO_2, $B_6C_2O_5$, and other B-C-O compounds are listed in Table 1. The calculated lattice parameters of B_2CO_2 and $B_6C_2O_5$ are in excellent agreement with the previous report [12], and the calculated lattice parameters of the other B-C-O compounds are also in excellent agreement with the previous report (see Table 1).

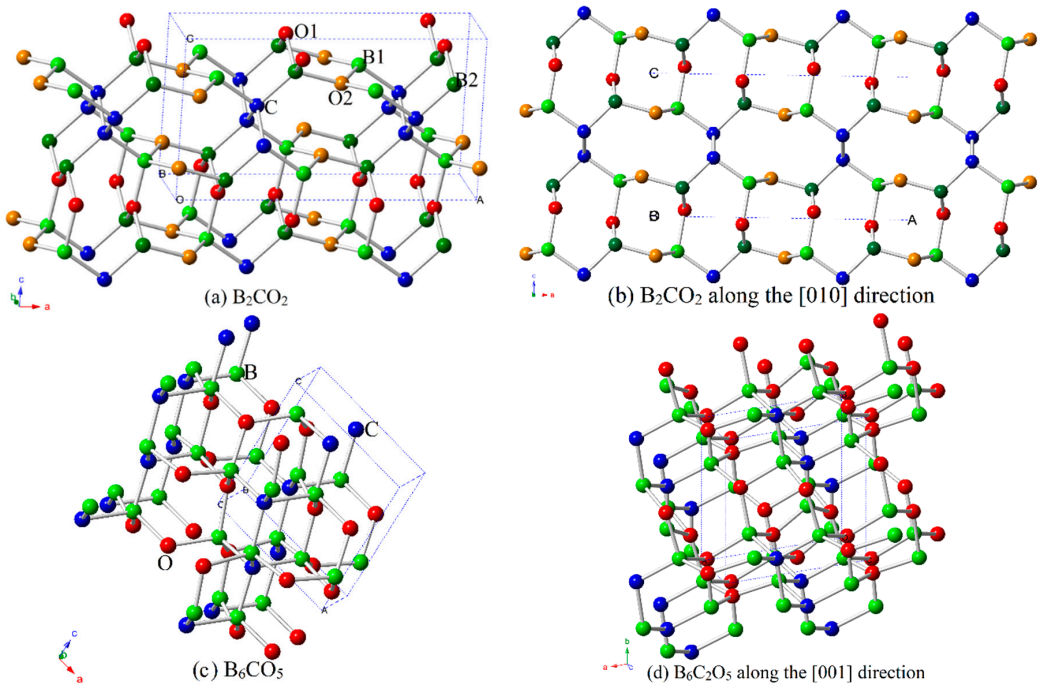

Figure 1. Lattice structure of B_2CO_2 (**a**); and along the [010] direction (**b**); and lattice structure of $B_6C_2O_5$ (**c**); and along the [001] direction (**d**).

Table 1. Calculated lattice parameters of B_2CO_2, $B_6C_2O_5$ and other B-C-O compounds.

Materials	Source	PBE				PBEsol				CA-PZ			
		a (Å)	*b* (Å)	*c* (Å)	*β* (°)	*a* (Å)	*b* (Å)	*c* (Å)	*β* (°)	*a* (Å)	*b* (Å)	*c* (Å)	*β* (°)
B_2CO_2	This work	9.773	2.487	5.395	90.9	9.721	2.479	5.368	90.8	9.606	2.456	5.308	90.9
	ref. [12]	9.776	2.489	5.395	90.8								
$B_6C_2O_5$	This work	4.503	4.536	4.557	98.1	4.479	4.526	4.508	99.3	4.278	4.474	4.457	99.3
	ref. [12]	4.502	4.538	4.557	98.2								
tP4-B_2CO	This work	2.656	2.656	3.678	90.0	2.648	2.648	3.656	90.0	2.618	2.618	3.619	90.0
	ref. [9]									2.623	2.623	3.623	90.0
tI16-B_2CO	This work	3.722	3.722	7.493	90.0	3.702	3.702	7.515	90.0	3.664	3.664	7.376	90.0
	ref. [9]									3.670	7.394	7.394	90.0
B_2C_2O	This work	2.638		18.274	90.0	2.627		18.178	90.0	2.598		17.996	90.0
	ref. [10]	2.647		18.272	90.0								

The relationships among the calculated lattice parameter ratios X/X_0 (a/a_0, b/b_0, c/c_0) and lattice volume ratios V/V_0 of B_2CO_2 and $B_6C_2O_5$ and pressure are shown in Figure 2, where a_0, b_0, c_0 and V_0 are the zero temperature and zero pressure equilibrium lattice constants and lattice volume, respectively. For B_2CO_2, it can be easily seen that the compression of the *b*-axis is the most difficult, whereas that of the *a*-axis is the easiest. For $B_6C_2O_5$, similar to B_2CO_2, the *b*-axis is the most difficult to

compress, while the *c*-axis is the easiest to compress. When the pressure increases, the compression along the *b*-axis of $B_6C_2O_5$ is much larger than that along the *b*-axis of B_2CO_2. In addition, it is found that the lattice constants b/b_0, c/c_0 compression of $B_6C_2O_5$ is changed at 10 GPa. This is because the lengths of some bonds decrease strongly along the lattice vector *b*-axis or the lattice vector *c*-axis. For example, there are three kinds of B-O bonds along the lattice vector *c*-axis; the bond lengths of B-O bonds are 1.571 Å (1.553 Å), 1.456 Å (1.459 Å) and 1.561 Å (1.543 Å) at 0 (5) GPa, respectively, and while the lengths of the first and the third bonds suddenly decreased to 1.516 Å and 1.508 Å under 10 GPa, the second bond length suddenly decreased to 1.489 Å under 10 GPa. Under 15 GPa, the first, second and third bond lengths dropped to 1.502 Å, 1.479 Å and 1.497 Å, respectively. From the above discussion, we can see that the abrupt change of the lattice constants c/c_0 compression of $B_6C_2O_5$ is due to the sudden decrease of the bond length of the B-O bonds along the lattice vector *c*-axis. The abrupt changes along the lattice vector *b*-axis is similar to that due to the abnormal change of the B-C bond length and the B-O bond. Their lattice constants changes show different trends with the pressure, which is related to the crystal structure and atomic composition. $B_6C_2O_5$ exists in the P1 space group, whereas B_2CO_2 is found in the C2/m space group and the P1 space group has the lowest symmetry among the 230 space groups. In Figure 2b, for the lattice volume ratio, we predict that B_2CO_2 has better compressive resistance than $B_6C_2O_5$. The results of Figure 2b confirm our prediction. Here, we can also predict that the bulk modulus of B_2CO_2 is greater than that of $B_6C_2O_5$.

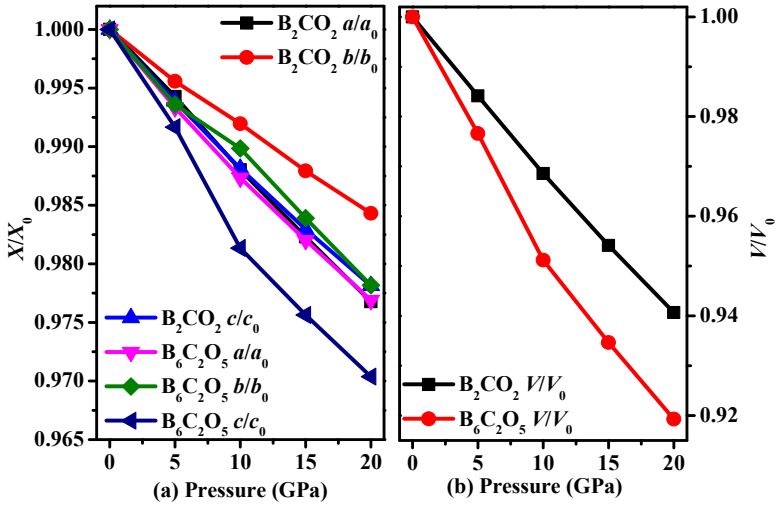

Figure 2. Lattice constants a/a_0, b/b_0, c/c_0 compression as functions of pressure for B_2CO_2 and $B_6C_2O_5$ (**a**); and primitive cell volume V/V_0 for B_2CO_2 and $B_6C_2O_5$ (**b**).

3.2. Stability

To demonstrate the dynamical stability of these compound, their phonon spectra are shown in Figure 3. At ambient pressure, there are no virtual frequencies in the entire Brillouin zone, proving that B_2CO_2 and $B_6C_2O_5$ are both dynamically stable. When P = 20 GPa, there are still no virtual frequencies in the entire Brillouin zone; in other words, B_2CO_2 and $B_6C_2O_5$ are still dynamically stable. The calculated elastic constants of B_2CO_2 and $B_6C_2O_5$ under different pressures are listed in Table 2. The calculated elastic constants of B_2CO_2 and $B_6C_2O_5$ at ambient pressure are in excellent agreement with the previously reported results [12]. There is no doubt that based on the data presented in Table 2, the elastic constants of B_2CO_2 and $B_6C_2O_5$ satisfy the mechanical stability criteria [45], indicating that B_2CO_2 and $B_6C_2O_5$ are mechanically stable. While dynamical and mechanical stabilities are verified by the phonon spectra and elastic constants, respectively, the formation enthalpy can be used to determine whether the new materials can be synthesized experimentally. Wang et al. have also described the possible synthetic routes of B_2CO_2 and $B_6C_2O_5$ in Ref. [12]. With regard to elastic

constants, compared to other B-C-O compounds, some elastic constants of B_2CO_2 and $B_6C_2O_5$ are larger and some are smaller.

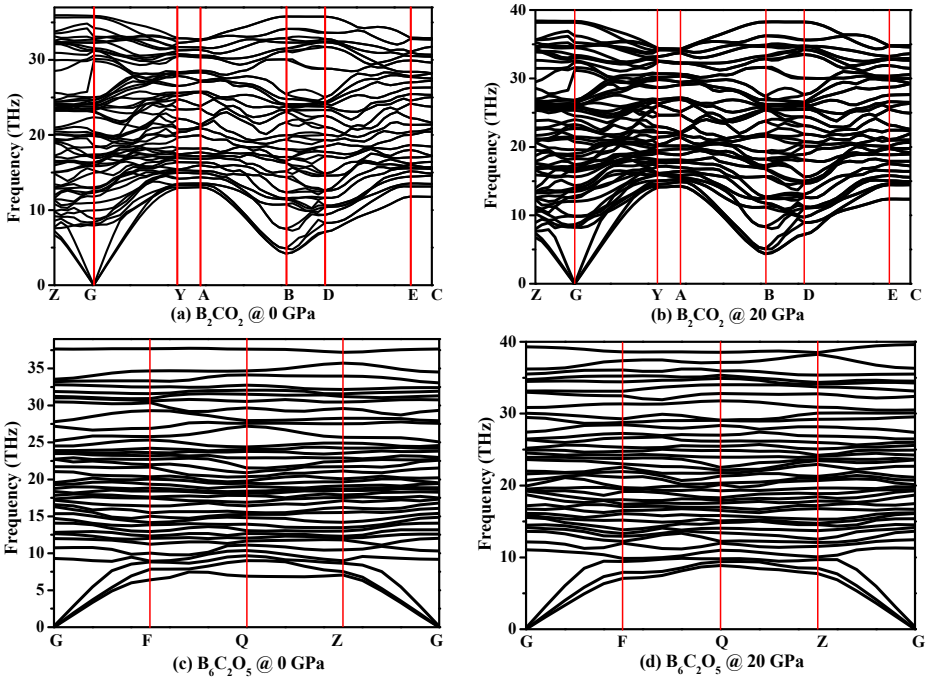

Figure 3. Phonon spectra of B_2CO_2 and $B_6C_2O_5$ under different pressures: B_2CO_2 @ 0 GPa (**a**); B_2CO_2 @ 20 GPa (**b**); $B_6C_2O_5$ @ 0 GPa (**c**); and $B_6C_2O_5$ @ 20 GPa (**d**).

Table 2. Calculated elastic constants (GPa) and elastic modulus (GPa) of B_2CO_2 and $B_6C_2O_5$ under different pressures (*P*: in GPa).

Materials	*P*	C_{11}	C_{22}	C_{33}	C_{44}	C_{55}	C_{66}	C_{12}	C_{13}	C_{23}	C_{15}	C_{25}	C_{35}	C_{46}	*B*	*G*	*E*
B_2CO_2	0	585	784	613	256	213	264	117	65	136	−77	13	51	−9	287	251	583
	5	622	813	649	267	221	269	125	82	145	−81	16	55	−10	306	260	608
	10	658	841	686	268	223	279	132	96	157	−85	15	57	−10	325	267	629
	15	694	872	718	274	226	281	141	110	168	−90	16	58	−13	344	273	648
	20	723	902	747	260	225	283	150	126	180	−95	13	64	−18	362	272	653
$B_6C_2O_5$	0	528	519	571	207	170	211	102	40	83	6	−0.2	−72	−8	227	203	469
	5	549	547	596	216	163	215	108	35	93	−10	−1	−87	−10	234	207	480
	10	640	534	631	233	191	237	131	81	122	26	6	−44	5	274	224	528
	15	665	573	665	243	204	245	142	91	133	31	8	−49	7	293	234	554
	20	704	613	697	258	210	259	155	104	142	35	11	−53	9	312	244	581
tP4-B_2CO	0 [1]	736		591	240		254	53	157						311	254	
tI16-B_2CO	0 [1]	600		646	304		283	182	144						310	265	
B_2C_2O	0 [2]	763		590	229		274	15	135						299	264	611
c-BN	0 [3]	779			446			165							370	384	
Pnma-BN	0 [4]	392	770	675	299	272	187	99	256	116					298	227	543
Diamond	0 [3]	1053			563			120							431	522	1116

[1] Reference [9]; [2] Reference [10]; [3] Reference [22]; [4] Reference [46].

3.3. Mechanical Properties and Elastic Anisotropy

The primary elastic constants and elastic modulus values of B_2CO_2 and $B_6C_2O_5$ as functions of pressure are shown in Figure 4, and the elastic modulus values for B_2CO_2, $B_6C_2O_5$ and other B-C-O compounds are also listed in Table 2. Inspection of Figure 4 shows that almost all primary elastic constants and elastic moduli increase with increasing pressure. For B_2CO_2, the rate of increase of the elastic constants and elastic moduli remains almost constant, while for $B_6C_2O_5$, the elastic constants and elastic moduli suddenly increase from 5 GPa to 10 GPa, and the rate of increase of elastic constants

and elastic moduli remains almost constant under other pressures. As is well-known, the elastic constant represents the elastic properties of a material. Elastic constants provide a description of the relationship of stress and strain of different directions in an anisotropic medium. The elastic constants also obey Hooke's law, and strain is proportional to stress, as expressed by Hooke's law $F = -kx$, where k is a constant, called the stiffness coefficient. The stiffness coefficient is a complex physical quantity related to the material itself and the external conditions such as the temperature, so that the changes in the elastic constants for $B_6C_2O_5$ observed in Figure 4c are also understandable. The lattice constant changes show different trends with the pressure, which are related to the differences in the crystal structure and atomic composition. $B_6C_2O_5$ is found in the $P1$ space group, while B_2CO_2 is found in the $C2/m$ space group, and the $P1$ space group has the lowest symmetry among the 230 space groups. For the $P1$ space group, there are 21 independent elastic constants, while for the $C2/m$ space group, there are only 13 independent elastic constants. The hardnesses of B_2CO_2 and $B_6C_2O_5$ were calculated by Wang et al. [11] using the Chen-Niu model [47] and the Lyakhov-Oganov model [48]. The results show that B_2CO_2 is a kind of superhard material. The Young's modulus E is calculated as: $E = 9BG/(3B + G)$. The calculated results for Young's modulus for B_2CO_2 and $B_6C_2O_5$ are also listed in Table 2. The Young's moduli of B_2CO_2 and $B_6C_2O_5$ increase with pressure, and the increase for $B_6C_2O_5$ is greater than that for B_2CO_2. The increase for $B_6C_2O_5$ was 23.88%, almost two times larger than that of B_2CO_2 (12.01%).

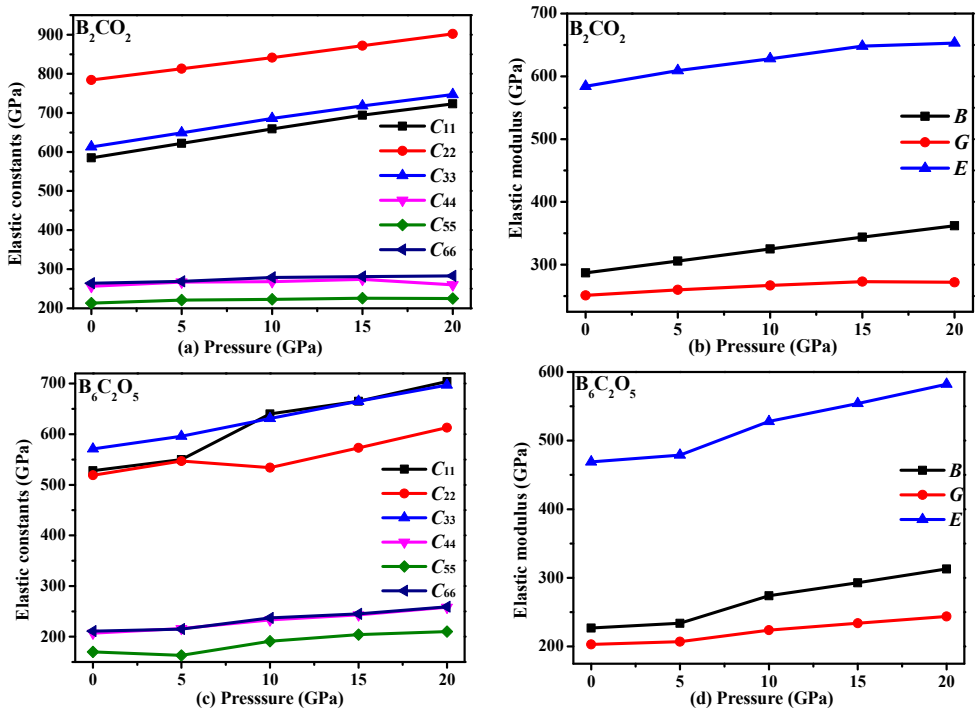

Figure 4. Elastic constants (**a**) and elastic modulus (**b**) as functions of pressure for B_2CO_2; and Elastic constants (**c**) and elastic modulus (**d**) as functions of pressure for $B_6C_2O_5$.

To analyze the anisotropy of B_2CO_2 and $B_6C_2O_5$ more systematically, the anisotropies of the shear moduli and Young's moduli of B_2CO_2 and $B_6C_2O_5$ are investigated using the ELAM codes [22,45,49]. To better understand the mechanical and anisotropic properties of B_2CO_2 and $B_6C_2O_5$, 3D surface figures of the shear moduli and Young's moduli for B_2CO_2 and $B_6C_2O_5$ are shown in Figure 5. The 3D surface figures represent the geometric figure that consists of the maximum or minimum value of the shear modulus or Young's modulus in all directions of space. The magnitude of the shear modulus or Young's modulus in all directions can be studied by using plane cutting, and the magnitude of the shear modulus or Young's modulus in any plane can be represented by a two-dimensional graph.

The 2D representations of the shear modulus and Young's modulus are shown in Figures 6 and 7, respectively. The 3D figure appears as a spherical shape for an isotropic material, while the deviation from the spherical shape is a measure of the degree of anisotropy [50]. It is clear that the shear and Young's moduli of B_2CO_2 and $B_6C_2O_5$ exhibit different degrees of anisotropy, and the anisotropies of the shear and Young's moduli of B_2CO_2 and $B_6C_2O_5$ increase with as the pressure increases from 0 GPa to 20 GPa. For example, a depression appears on the minimum value surface (green surface) of the shear modulus of B_2CO_2 at 20 GPa (see Figure 5b), but there is no dent under ambient pressure. In another example, at 20 GPa, a distinct dent appears on the three-dimensional Young's modulus surface for $B_6C_2O_5$ (see Figure 5h). Similarly, the indentation on the three-dimensional Young's modulus surface for $B_6C_2O_5$ is not so obvious at ambient pressure.

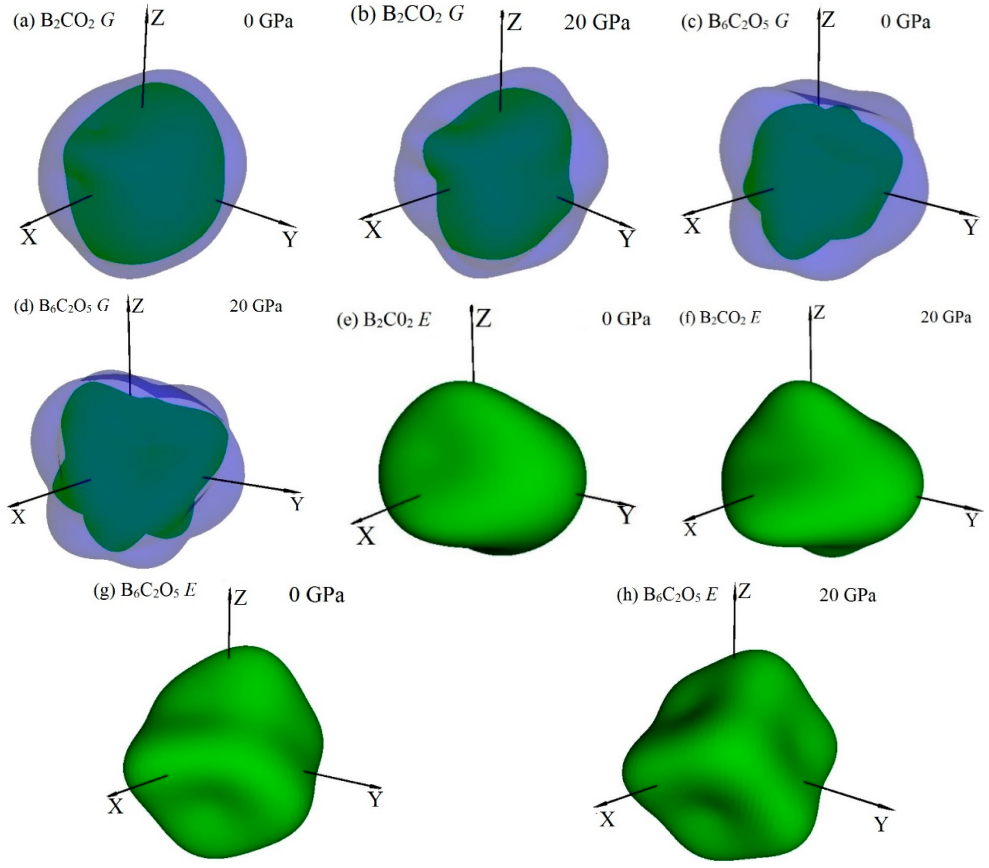

Figure 5. Directional dependence of the shear modulus at 0 GPa (**a**) and 20 GPa (**b**), and Young's modulus at 0 GPa (**c**) and 20 GPa (**d**) of B_2CO_2; and Directional dependence of the shear modulus at 0 GPa (**e**) and 20 GPa (**f**), and Young's modulus at 0 GPa (**g**) and 20 GPa (**h**) of $B_6C_2O_5$.

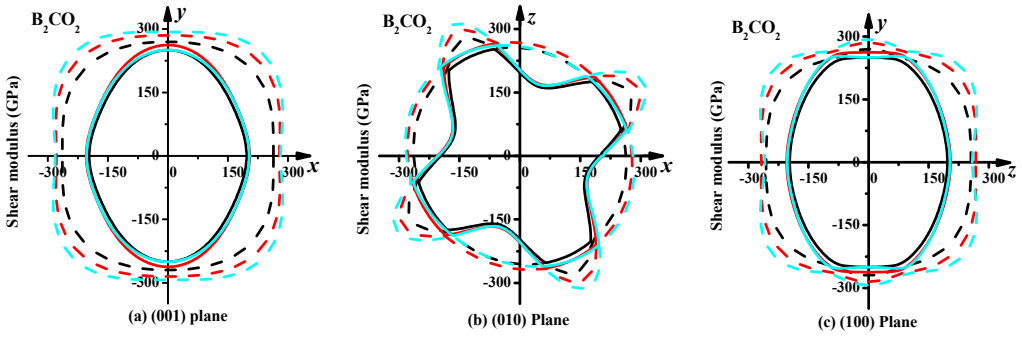

Figure 6. *Cont.*

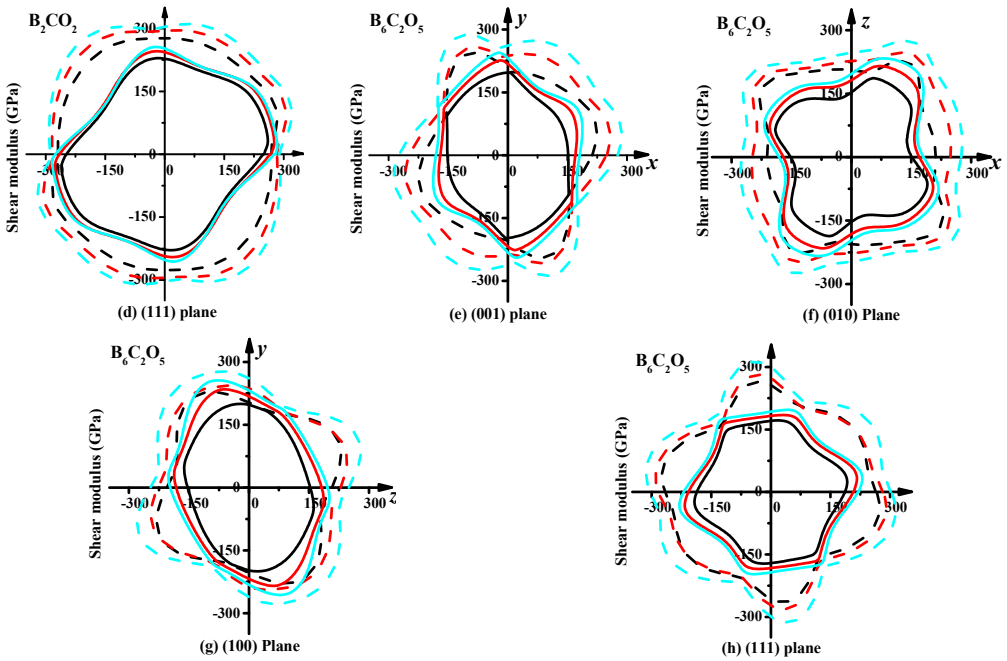

Figure 6. Planar projections of the directional dependence of the shear modulus in B_2CO_2, (**a**): (001) plane, (**b**): (010) plane, (**c**): (100) plane, and (**d**): (111) plane; and Planar projections of the directional dependence of the shear modulus in $B_6C_2O_5$, (**e**): (001) plane, (**f**): (010) plane, (**g**): (100) plane, and (**h**): (111) plane.

The sectional profiles are constructed on the basis of analysis of the geometrical characteristics of the 3D surfaces of the shear and Young's moduli of B_2CO_2 and $B_6C_2O_5$. Sectional drawings of the shear and Young's moduli are shown in Figures 6 and 7, respectively. The black, red and cyan lines represent the shear moduli at 0, 10 and 20 GPa, while the dash-dotted line and the solid line represent the maximum and minimum values of the shear modulus along different directions in the (001) plane (*xy* plane), (010) plane (*xz* plane), (100) plane (*yz* plane) and (111) plane, respectively. As shown in Figure 6, the anisotropy of B_2CO_2 and $B_6C_2O_5$ in the shear modulus increases with increasing pressure. Examination of Figure 6a shows that along the direction of the *x*-axis, the maximum values of shear modulus shrink inwards at 20 GPa, but the maximum values of the shear modulus remain constant in the direction of the *x*-axis at ambient pressure. According to the geometrical shape of the profile, the anisotropy of $B_6C_2O_5$ in the shear modulus is larger than that of B_2CO_2 at ambient pressure, while under high pressure, the anisotropy of $B_6C_2O_5$ is smaller than that of B_2CO_2. This can be proved by comparing the ratio of the maximum to the minimum of the shear modulus (G_{max}/G_{min}). The maximum and the minimum values of the shear modulus and Young's modulus for B_2CO_2 and $B_6C_2O_5$ are listed in Table 3. The maximum value of shear modulus for B_2CO_2 increases with pressure, while the minimum value of the shear modulus for B_2CO_2 increases first and then decreases with pressure, so that the anisotropy of B_2CO_2 in the shear modulus becomes increasingly large. The anisotropy of $B_6C_2O_5$ in the shear modulus decreases first and then increases.

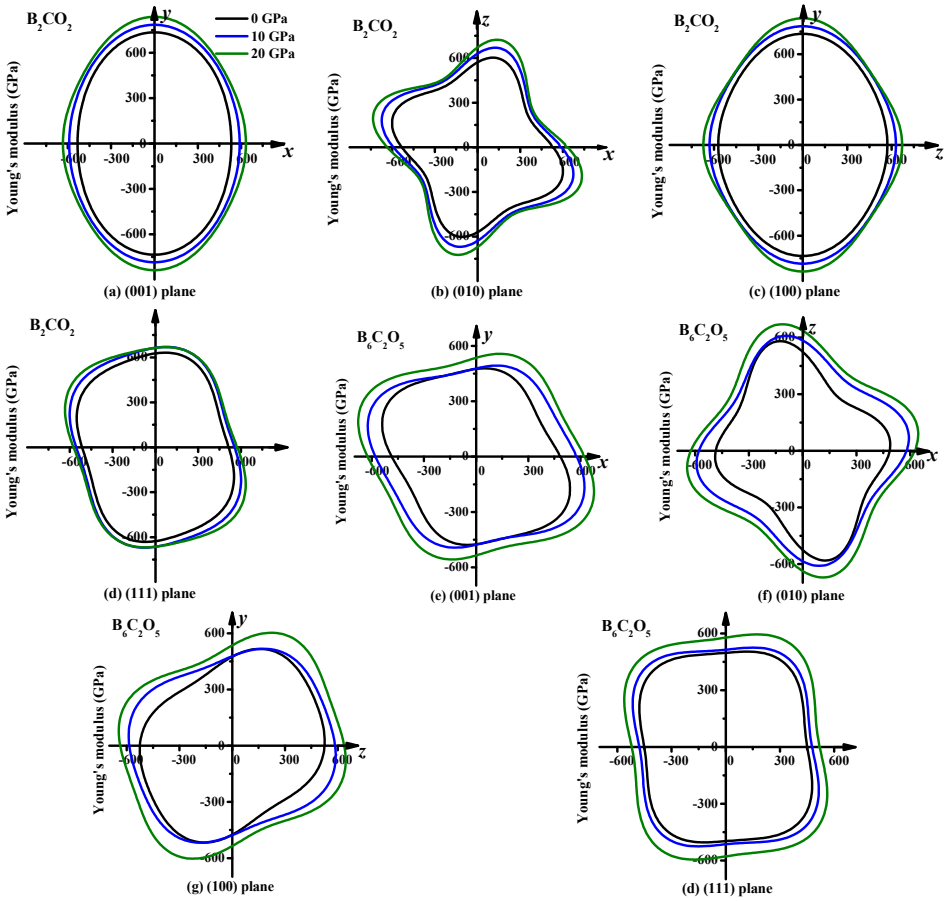

Figure 7. Planar projections of the directional dependence of the Young's modulus in B_2CO_2, (**a**): (001) plane, (**b**): (010) plane, (**c**): (100) plane, and (**d**): (111) plane; and Planar projections of the directional dependence of the Young's modulus in $B_6C_2O_5$, (**e**): (001) plane, (**f**): (010) plane, (**g**): (100) plane, and (**h**): (111) plane.

Table 3. Calculated the maximum values (in GPa) and minimum values (in GPa) of Young's modulus and shear modulus and the X_{max}/X_{min} ratio for B_2CO_2 and $B_6C_2O_5$.

Materials	*P*	0 GPa			10 GPa			20 GPa		
		Max	Min	Ratio	Max	Min	Ratio	Max	Min	Ratio
B_2CO_2	*G*	309	170	1.82	333	177	1.88	353	175	2.02
	E	734	414	1.77	785	446	1.76	837	460	1.82
$B_6C_2O_5$	*G*	278	140	1.96	295	161	1.83	321	170	1.88
	E	603	345	1.75	657	408	1.61	717	431	1.66

The 2D representations of the Young's moduli of B_2CO_2 and $B_6C_2O_5$ in the (001) plane (*xy* plane), (010) plane (*xz* plane), (100) plane (*yz* plane) and (111) plane are displayed in Figure 7a–h, respectively. The anisotropy of Young's modulus at each plane is also different, taking B_2CO_2 as an example. The Young's modulus in the (010) plane (E_{max}/E_{min} = 628 GPa/414 GPa = 1.52) of B_2CO_2 exhibits the largest anisotropy compared to the other planes, while the (100) plane (E_{max}/E_{min} = 734 GPa/571 GPa = 1.29) exhibits the smallest anisotropy. This result can also be demonstrated by the ratio of the maximum to the minimum of the Young's modulus at each plane. The maximum values of Young's modulus for B_2CO_2 appear in the (001) plane and (100) plane, while the minimum value of Young's modulus appears in the (010) plane. The maximum and minimum values appear in the same plane, whether at ambient pressure or at high pressure. Another interesting phenomenon is that the

anisotropy of Young's modulus in the (001) plane decreases with increasing pressure, and that of the (010) plane increases with increasing pressure, while those of the (100) plane and (111) plane decrease first and then increase. For the whole material, the anisotropies of the Young's moduli of B_2CO_2 and $B_6C_2O_5$ decrease first and then increase. In addition, although the maximum and minimum values appear in the same plane, whether at ambient pressure or at high pressure, the direction is changed. For $B_6C_2O_5$, the maximum value appears at $\theta = 2.82$, $\phi = 5.93$ (the two angles are used to describe the unit vector, which is fully characterized by the angles θ $(0, \pi)$, ϕ $(0, 2\pi)$, as explained in more detail in Refs. [48,49]) at ambient pressure, where the angle is in radians. While the maximum value appears at $\theta = 1.59$, $\phi = 2.90$ at 10 GPa, for the pressure of 20 GPa, the maximum value appears at $\theta = 1.55$, $\phi = 2.73$. At these three pressures (0 GPa, 10 GPa, 20 GPa), the direction of the minimum appears to be different. However, for B_2CO_2, the maximum values all appear at $\theta = 1.57$, $\phi = 4.73$, whether at ambient pressure or at high pressure, but the direction of the minimum appears to have changed.

3.4. Electronic Properties

The electronic band structure is a significant physical property of a material that can be used to determine whether the material is a semiconductor, metal, or insulator. The electronic band structures of B_2CO_2 and $B_6C_2O_5$ under different pressures are illustrated in Figure 8a–d, respectively. In Figure 8a–d, it is clear that B_2CO_2 and $B_6C_2O_5$ are both indirect and wide band gap semiconductor materials with the band gaps of 5.63 and 5.24 eV, respectively. For $B_6C_2O_5$, the conduction band minimum (CBM) and valence band maximum (VBM) are both located at the Dirac points in the Brillouin zone, the CBM of B_2CO_2 is also located at the Dirac point in the Brillouin zone, while the VBM of B_2CO_2 is not at the Dirac point in the Brillouin zone. The CBM and VBM are both located at the Q and F points in the Brillouin zone for $B_6C_2O_5$, and the CBM of B_2CO_2 is also located at the V point in the Brillouin zone, while the VBM of B_2CO_2 is located at $(-0.5000, -0.2143, 0.5000)$ along the L-M direction (L: $(-0.5, 0.0, 0.5)$; M: $(-0.5, -0.5, 0.5)$) in the Brillouin zone.

The band gaps of B_2CO_2 and $B_6C_2O_5$ under different pressures are shown in Figure 8e. The two materials show different trends for the change of the band gap with increasing pressure. The band gap of $B_6C_2O_5$ increases with pressure, while the band gap of B_2CO_2 first increases and then decreases. The change trend of the band gap of $B_6C_2O_5$ is similar to that of diamond and c-BN [22]: the band gap of $B_6C_2O_5$, diamond and c-BN all increase with increasing pressure, but the changes for the band gaps of diamond and c-BN are relatively smooth, and the band gap changes for $B_6C_2O_5$ are quite abrupt. Then, we investigated the origin of the pressure-driven abrupt increase of the band and the non-monotonic trend of first increase and then decrease of the band gap for $B_6C_2O_5$ and B_2CO_2, respectively. We analyzed the trend in the Fermi level and the conduction band minimum with the change of pressure. The relationships between the Fermi level and the conduction band minimum for B_2CO_2 and $B_6C_2O_5$ and the pressure are shown in Figure 8f. For the Fermi level and the conduction band minimum of B_2CO_2 and the conduction band minimum of $B_6C_2O_5$, the changes are relatively smooth, but the energy at the CBM of $B_6C_2O_5$ increases abruptly from 0 GPa to 5 GPa and from 5 GPa to 10 GPa. Therefore, the band gaps of $B_6C_2O_5$ changes abruptly due to the sudden increase in the energy at the CBM leading to a sudden increase of the band gap from 5.309 eV under 5 GPa to 5.549 eV under 10 GPa.

To better understand why the band gap of $B_6C_2O_5$ becomes larger with increased pressure, we also analyze the density of states of $B_6C_2O_5$. The densities of states of $B_6C_2O_5$ under different pressures are shown in Figure 9. Examination of Figure 9a shows that the valence band moves towards low energy, while the conduction band moves towards high energy in the 0–20 GPa range, so that the band gap of $B_6C_2O_5$ increases with increased pressure. However, as shown in Figure 8e, the Fermi level increases with increased pressure, so, why does the band gap of $B_6C_2O_5$ increase with the pressure in the 0–20 GPa range? According to Figure 9c, the density of states of the carbon atom almost does not vary with the pressure. Figure 9 b,d shows that, considering the density of states distribution of the oxygen atom, the peak value of the oxygen contribution to the conduction band increases with

the increasing pressure, indicating that for the oxygen atoms under the action of external pressure, the local energy level is higher, resulting in reduced oxygen ions and leading to further changes of the band gap. Further consideration of the B atoms shows that the peak density of states increases with increasing pressure, decreasing the degree of localization of these atoms; however, the decrease in the density of states (from 1.07 state/eV/fu to 0.82 state/eV/fu when the pressure increases from 5 GPa to 10 GPa) is much smaller than the increase in the degree of the O atom localization (from 1.62 state/eV/fu to 3.24 state/eV/fu when the pressure increases from 5 GPa to 10 GPa), so that the results showed that the band gap of $B_6C_2O_5$ becomes larger.

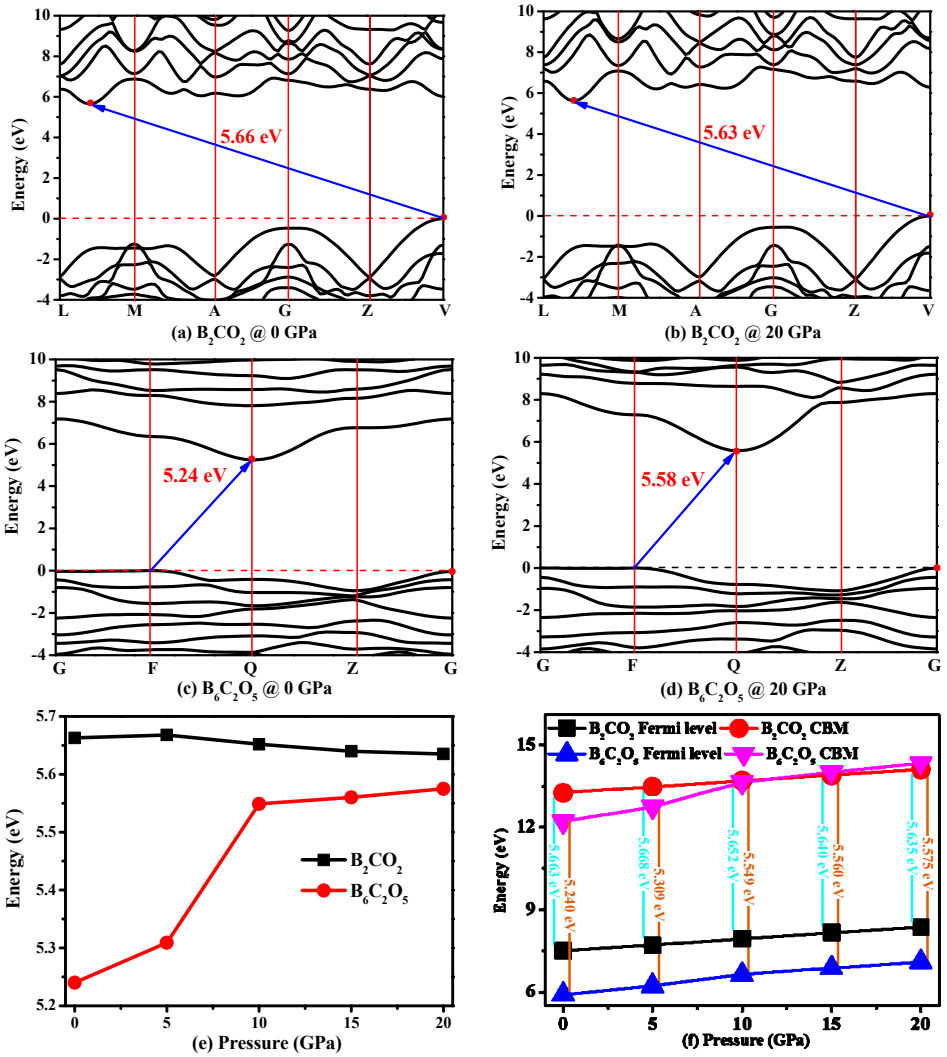

Figure 8. Band structures of: B_2CO_2 ((**a**): 0 GPa; and (**b**): 20 GPa); and $B_6C_2O_5$ (**c**): 0 GPa; and (**d**): 20 GPa); band gaps as functions of pressure for B_2CO_2 and $B_6C_2O_5$ (**e**); and Fermi level and CBM as functions of pressure for B_2CO_2 and $B_6C_2O_5$ (**f**).

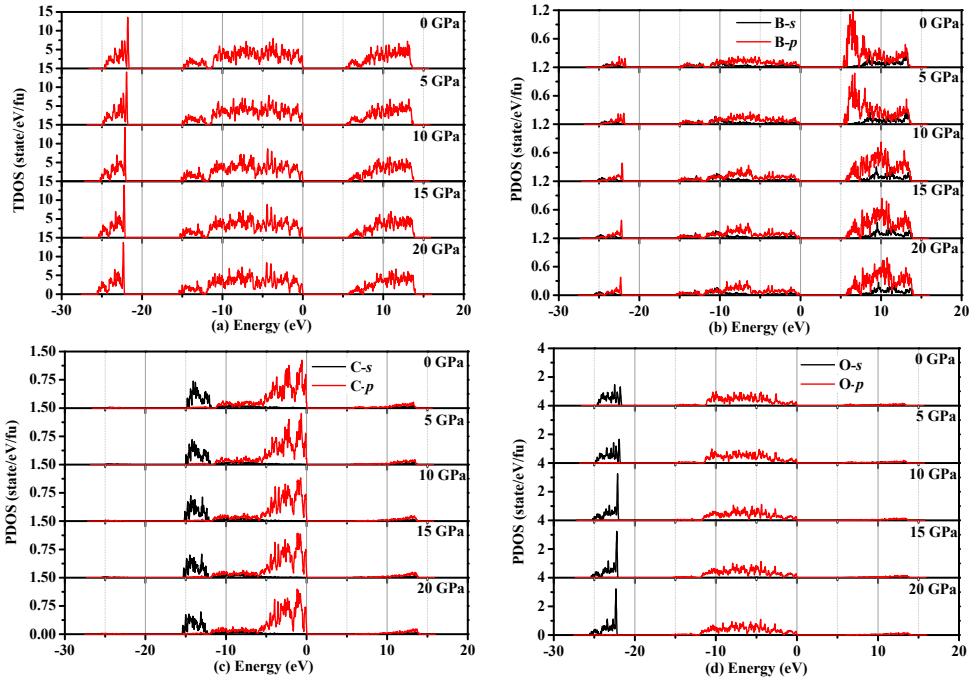

Figure 9. Density of states of $B_6C_2O_5$ under different pressures: total density of states (**a**); partial density of states of B atom (**b**); partial density of states of C atom (**c**); and partial density of states of O atom (**d**).

4. Conclusions

Based on first-principles calculations, we have systematically investigated two ternary light element compounds, $B_6C_2O_5$ and B_2CO_2. We find that such two sp^2 and sp^3 hybridized structures could be obtained by other compounds and elements and that these structures are dynamically stable through calculations of the phonon spectra for $B_6C_2O_5$ and B_2CO_2. The electronic band structures are also calculated, showing that B_2CO_2 and $B_6C_2O_5$ are wide-gap semiconductor materials with indirect energy gaps of approximately 5.66 and 5.24 eV, respectively. The elastic anisotropy of B_2CO_2 and $B_6C_2O_5$ phase has been demonstrated by the Young's modulus and shear modulus along different crystal orientations. The elastic anisotropy results show that $B_6C_2O_5$ exhibits a larger anisotropy in the shear modulus, while B_2CO_2 exhibits a larger anisotropy in Young's modulus at ambient pressure. Another interesting phenomenon is that the anisotropy of the shear modulus of B_2CO_2 increases with increasing pressure, while the anisotropy of Young's modulus of B_2CO_2, and the anisotropy of Young's modulus and the shear modulus of $B_6C_2O_5$ all first decrease and then increase with increasing pressure. The changes of the physical properties of B_2CO_2 and $B_6C_2O_5$ show different trends with the pressure, and are strongly related to the crystal structure and atomic composition. The origin of band gap increases with increased pressure is explained from the viewpoint of the density of states. In addition, hardness calculations using the Lyakhov-Oganov model show that B_2CO_2 is a potential superhard material.

Acknowledgments: This work was supported by the National Natural Science Foundation of China (No. 61762082), and Scientific Research Program of Shaanxi Education Department: Research and Design of Novel B-C-O Superhard Material. Wei Zhang (School of Microelectronics, Xidian University) is thanked for allowing to use the CASTEP code in Materials Studio.

Author Contributions: Liping Qiao designed the project; Liping Qiao and Zhao Jin performed the calculations; Liping Qiao and Zhao Jin determined the results; and Liping Qiao wrote the manuscript.

Conflicts of Interest: The authors declare no conflict of interest.

References

1. Shirai, K.; Sakuma, K.; Uemura, N. Theoretical study of the structure of boron carbide $B_{13}C_2$. *Phys. Rev. B* **2014**, *90*, 064109. [CrossRef]
2. Ektarawong, A.; Simak, S.I.; Hultman, L.; Birch, J.; Tasnádi, F.; Wang, F.; Alling, B. Effects of configurational disorder on the elastic properties of icosahedral boron-rich alloys based on B_6O, $B_{13}C_2$, and B_4C, and their mixing thermodynamics. *J. Chem. Phys.* **2016**, *144*, 134503. [CrossRef] [PubMed]
3. Wang, J.J.; Wang, Z.Y.; Jing, Y.Y.; Wang, S.Y.; Chou, C.F.; Hu, H.; Chiou, S.H.; Tsoo, C.C.; Su, W.S. Electronic structure and optical properties of boron suboxide B_6O system: First-principles investigations. *Solid State Commun.* **2016**, *244*, 12–16. [CrossRef]
4. Wang, D.Y.; Yan, Q.; Wang, B.; Wang, X.Y.; Yang, J.M.; Yang, G. Predicted boron-carbide compounds: A first-principles study. *J. Chem. Phys.* **2014**, *140*, 224704. [CrossRef] [PubMed]
5. Fan, Q.Y.; Wei, Q.; Chai, C.C.; Yan, H.Y.; Zhang, M.G.; Zhang, Z.X.; Zhang, J.Q.; Zhang, D.Y. Structural, anisotropic and thermodynamic properties of boron carbide: First principles calculations. *Indian J. Pure Appl. Phys.* **2016**, *54*, 227–235.
6. Fan, Q.Y.; Wei, Q.; Chai, C.C.; Yu, X.Y.; Liu, Y.; Zhou, P.K.; Yan, H.T.; Zhang, D.Y. First-principles study of structural, elastic, anisotropic, and thermodynamic properties of R_3-B_2C. *Chin. J. Phys.* **2015**, *53*, 100601. [CrossRef]
7. Fan, Q.Y.; Wei, Q.; Chai, C.C.; Yang, Y.T.; Yu, X.H.; Liu, Y.; Zheng, J.P.; Zhou, P.K.; Zhang, D.Y. The elastic anisotropic and thermodynamic properties of *I*4*mm*-B_3C. *Acta Phys. Pol. A* **2016**, *129*, 103–108. [CrossRef]
8. Liu, C.; Zhao, Z.S.; Luo, K.; Hu, M.; Ma, M.D.; He, J.L. Superhard orthorhombic phase of B_2CO compound. *Diam. Relat. Mater.* **2017**, *73*, 7–92. [CrossRef]
9. Li, Y.W.; Li, Q.; Ma, Y.M. B_2CO: A potential superhard material in the B-C-O system. *EPL* **2011**, *95*, 66006. [CrossRef]
10. Zhang, M.G.; Yan, H.Y.; Zheng, B.B.; Wei, Q. Influences of carbon concentration on crystal structures and idealstrengths of B_2C_xO compounds in the B-C-O system. *Sci. Rep.* **2015**, *5*, 15481. [CrossRef] [PubMed]
11. Zheng, B.B.; Zhang, M.G.; Wang, C.J. Exploring the mechanical anisotropy and ideal strengths of tetragonal B_4CO_4. *Materials* **2017**, *10*, 128. [CrossRef] [PubMed]
12. Wang, S.N.; Oganov, A.R.; Qian, G.R.; Zhu, Q.; Dong, H.F.; Dong, X.; Esfahani, M.M.D. Novel superhard B-C-O phases predicted from first principles. *Phys. Chem. Chem. Phys.* **2016**, *18*, 1859–1863. [CrossRef] [PubMed]
13. Zhou, S.; Zhao, J.J. Two-dimensional B-C-O alloys: A promising 2D material for electronic devices. *Nanoscale* **2016**, *8*, 8910–8918. [CrossRef] [PubMed]
14. Zhao, Y.; He, D.W.; Daemen, L.L.; Shen, R.B.; Schwarz, R.B.; Zhu, Y.; Bish, D.L.; Hung, J.; Zhang, J.; Shen, G.; et al. Superhard B-C-N materials synthesized in nanostructured bulks. *J. Mater. Res.* **2002**, *17*, 3139–3145. [CrossRef]
15. He, J.L.; Tian, Y.J.; Yu, D.L.; Wang, T.S.; Liu, S.M.; Guo, L.C.; Li, D.C.; Jia, X.P.; Chen, L.X.; Zou, G.T.; et al. Orthorhombic B_2CN crystal synthesized by high pressure and temperature. *Chem. Phys. Lett.* **2001**, *340*, 431–436. [CrossRef]
16. Nakano, S.; Akaishi, M.; Sasaki, T.; Yamaoka, S. Segregative crystallization of several diamond-like phases from the graphitic BC_2N without an additive at 7.7 GPa. *Chem. Mater.* **1994**, *6*, 2246–2251. [CrossRef]
17. Knittle, E.; Kaner, R.B.; Jeanloz, R.; Cohen, M.L. High-pressure synthesis, characterization, and equation of state of cubic C-BN solid solutions. *Phys. Rev. B* **1995**, *51*, 12149. [CrossRef]
18. Solozhenko, V.L.; Andrault, D.; Fiquet, G.; Mezouar, M.; Rubie, D.C. Synthesis of superhard cubic BC_2N. *Appl. Phys. Lett.* **2001**, *78*, 1385–1387. [CrossRef]
19. Komatsu, T.; Nomura, M.; Kakudate, Y.; Fujiwara, S. Synthesis and characterization of a shock-synthesized cubic B-C-N solid solution of composition $BC_{2.5}N$. *J. Mater. Chem.* **1996**, *6*, 1799–1803. [CrossRef]
20. Zhang, X.X.; Wang, Y.C.; Lv, J.; Zhu, C.Y.; Li, Q.; Zhang, M.; Li, Q.; Ma, Y.M. First-principles structural design of superhard materials. *J. Chem. Phys.* **2013**, *138*, 114101. [CrossRef] [PubMed]
21. Fan, Q.Y.; Wei, Q.; Chai, C.C.; Zhang, M.G.; Yan, H.Y.; Zhang, Z.X.; Zhang, J.Q.; Zhang, D.Y. Elastic and electronic properties of Imm2- and I-4m2-BCN. *Comput. Mater. Sci.* **2015**, *97*, 6–13. [CrossRef]

22. Fan, Q.Y.; Wei, Q.; Chai, C.C.; Yan, H.Y.; Zhang, M.G.; Lin, Z.Z.; Zhang, Z.X.; Zhang, J.Q.; Zhang, D.Y. Structural, mechanical, and electronic properties of P3m1-BCN. *J. Phys. Chem. Solids* **2015**, *79*, 89–96. [CrossRef]
23. Fan, Q.Y.; Wei, Q.; Yan, H.Y.; Zhang, M.G.; Zhang, Z.X.; Zhang, J.Q.; Zhang, D.Y. Elastic and electronic properties of Pbca-BN: First-principles calculations. *Comput. Mater. Sci.* **2014**, *85*, 80–87. [CrossRef]
24. He, D.W.; Zhao, Y.S.; Daemen, L.; Qian, J.; Shen, T.D. Boron suboxide: As hard as cubic boron nitride. *Appl. Phys. Lett.* **2002**, *81*, 643–645. [CrossRef]
25. Endo, T.; Sato, T.; Shimada, M. High-pressure synthesis of B_2O with diamond-like structure. *J. Mater. Sci. Lett.* **1987**, *6*, 683–685. [CrossRef]
26. Solozhenko, V.L.; Kurakevych, O.O.; Turkevich, V.Z.; Turkevich, D.V. Phase diagram of the B-B_2O_3 system at 5 GPa: Experimental and theoretical studies. *J. Phys. Chem. B* **2008**, *112*, 6683–6687. [CrossRef] [PubMed]
27. Gueorguiev, G.K.; Neidhardt, J.; Stafstrom, S.; Hultman, L. First-principles calculations on the role of CN precursors for the formation of fullerene-like carbon nitride. *Chem. Phys. Lett.* **2005**, *401*, 288–295. [CrossRef]
28. Gueorguiev, G.K.; Neidhardt, J.; Stafstrom, S.; Hultman, L. First-principles calculations on the curvature evolution and cross-linkage in carbon nitride. *Chem. Phys. Lett.* **2005**, *410*, 228–234. [CrossRef]
29. Liu, A.Y.; Cohen, M.L. Prediction of new low compressibility solids. *Science* **1989**, *245*, 841–842. [CrossRef] [PubMed]
30. Liu, A.Y.; Wentzcovitch, R.M. Stability of carbon nitride solids. *Phys. Rev. B* **1994**, *50*, 10362. [CrossRef]
31. Teter, D.M.; Hemley, R.J. Low-compressibility carbon nitrides. *Science* **1996**, *271*, 53–55. [CrossRef]
32. Manyali, G.S.; Warmbier, R.; Quandt, A.; Lowther, J.E. Ab initio study of elastic properties of super hard and graphitic structures of C_3N_4. *Comput. Mater. Sci.* **2013**, *69*, 299–303. [CrossRef]
33. Molina, B.; Sansores, L.E. Eelectronic structure of six phases of C_3N_4: A theoretical approach. *Mod. Phys. Lett. B* **1999**, *13*, 193–201. [CrossRef]
34. Zhao, J.; Fan, C. First-principles study on hardness of five polymorphs of C_3N_4. *Phys. B Condens. Matter* **2008**, *403*, 1956–1959. [CrossRef]
35. Fan, Q.Y.; Chai, C.C.; Wei, Q.; Yang, Y.T. Two Novel C_3N_4 Phases: Structural, Mechanical and Electronic Properties. *Materials* **2016**, *9*, 427. [CrossRef] [PubMed]
36. Gao, F.M.; He, J.L.; Wu, E.; Liu, S.M.; Yu, D.L.; Li, D.C.; Zhang, S.Y.; Tian, Y.J. Hardness of covalent crystals. *Phys. Rev. Lett.* **2003**, *91*, 015502. [CrossRef] [PubMed]
37. Perdew, J.P.; Burke, K.; Ernzerhof, M. Generalized gradient approximation made simple. *Phys. Rev. Lett.* **1996**, *77*, 3865. [CrossRef] [PubMed]
38. Perdew, J.P.; Ruzsinszky, A.; Csonka, G.I.; Vydrov, O.A.; Scuseria, G.E.; Constantin, L.A.; Zhou, X.L.; Burke, K. Erratum: Restoring the density-gradient expansion for exchange in solids and surfaces. *Phys. Rev. Lett.* **2009**, *102*, 039902. [CrossRef]
39. Ceperley, D.M.; Alder, B.J. Ground state of the electron gas by a stochastic method. *Phys. Rev. Lett.* **1980**, *45*, 566. [CrossRef]
40. Perdew, J.P.; Zunger, A. Self-interaction correction to density-functional approximations for many-electron systems. *Phys. Rev. B* **1981**, *23*, 5048. [CrossRef]
41. Clark, S.J.; Segall, M.D.; Pickard, C.J.; Hasnip, P.J.; Probert, M.I.J.; Refson, K.; Payne, M.C. First principles methods using CASTEP. *Z. Kristallogr.* **2005**, *220*, 567–570. [CrossRef]
42. Pfrommer, B.G.; Côté, M.; Louie, S.G.; Cohen, M.L. Relaxation of crystals with the quasi-newton method. *J. Comput. Phys.* **1997**, *131*, 233–240. [CrossRef]
43. Monkhorst, H.J.; Pack, J.D. Special points for Brillouin-zone integrations. *Phys. Rev. B* **1976**, *13*, 5188. [CrossRef]
44. Krukau, A.V.; Vydrov, O.A.; Izmaylov, A.F.; Scuseria, G.E. Influence of the exchange screening parameter on the performance of screened hybrid functionals. *J. Chem. Phys.* **2006**, *125*, 224106. [CrossRef] [PubMed]
45. Ma, Z.Y.; Han, Z.; Liu, X.H.; Yu, X.H.; Wang, D.T.; Tian, Y. *Pnma*-BN: Another boron nitride polymorph with interesting physical properties. *Nanomaterials* **2017**, *7*, 3. [CrossRef] [PubMed]
46. Nye, J.F. *Physical Properties of Crystals*; Oxford University Press: Oxford, UK, 1985.
47. Chen, X.Q.; Niu, H.Y.; Li, D.Z.; Li, Y.Y. Modeling hardness of polycrystalline materials and bulk metallic glasses. *Intermetallics* **2011**, *19*, 1275–1281. [CrossRef]
48. Lyakhov, A.O.; Oganov, A.R. Evolutionary search for superhard materials: Methodology and applications to forms of carbon and TiO_2. *Phys. Rev. B* **2011**, *84*, 092103. [CrossRef]

49. Marmier, A.; Lethbridge, Z.A.D.; Walton, R.I.; Smith, C.W.; Parker, S.C.; Evans, K.E. Elam: A computer program for the analysis and representation of anisotropic elastic properties. *Comput. Phys. Commun.* **2010**, *181*, 2102–2115. [CrossRef]
50. Hu, W.C.; Liu, Y.; Li, D.J.; Zeng, X.Q.; Xu, C.S. First-principles study of structural and electronic properties of C_{14}-type laves phase Al_2Zr and Al_2Hf. *Comput. Mater. Sci.* **2014**, *83*, 27–34. [CrossRef]

© 2017 by the authors. Licensee MDPI, Basel, Switzerland. This article is an open access article distributed under the terms and conditions of the Creative Commons Attribution (CC BY) license (http://creativecommons.org/licenses/by/4.0/).